Publication I

Hyvönen, N., and Seiskari, O. **Detection of multiple inclusions from sweep data of electrical impedance tomography.** ***Inverse Problems*****, Vol. 28, 095014 (22 pp.), 2012.**

IOP Publishing Inverse Problems

Inverse Problems **28** (2012) 095014 (22pp) doi:10.1088/0266-5611/28/9/095014

Detection of multiple inclusions from sweep data of electrical impedance tomography

Nuutti Hyvönen and Otto Seiskari

Department of Mathematics and Systems Analysis, Aalto University, PO Box 11100, FI-00076 Aalto, Finland

E-mail: nuutti.hyvonen@aalto.fi and otto.seiskari@aalto.fi

Received 16 April 2012, in final form 18 July 2012
Published 24 August 2012
Online at stacks.iop.org/IP/28/095014

Abstract

This paper considers detection of conductivity inhomogeneities inside an otherwise homogeneous object by electrical impedance tomography using only two electrodes: one of the electrodes is held fixed, while the other moves around the examined object. Unit current is maintained between the electrodes, and the corresponding (relative) potential difference is measured as a function of the position of the dynamic electrode, thus producing so-called sweep data. In two dimensions and with point-like electrodes, the sweep data have previously been shown to extend as a holomorphic function to the exterior of the inhomogeneities. We derive a holomorphic asymptotic expansion for the (extended) sweep data with respect to the size of Lipschitz inclusions with constant conductivity levels. Based on this result, we subsequently introduce a numerical algorithm that locates the inclusions and estimates their strengths by considering the poles and corresponding residues of suitable Laurent–Padé approximants of the sweep data. The functionality of the reconstruction technique is demonstrated via numerical experiments, some of which are three dimensional and/or based on simulated complete electrode model measurements.

1. Introduction

The objective of electrical impedance tomography (EIT) is to deduce information about the conductivity distribution inside a physical body from measurements of current and voltage on its boundary. EIT has applications in, e.g., medical imaging, process tomography and nondestructive testing of materials; see [8, 10, 29] and the references therein. In this work, we consider a special configuration of EIT where the measurements are performed with two electrodes and the aim is to detect inclusions inside an otherwise homogeneous object. This task could correspond to, e.g., inferring whether a piece of building material contains cracks, impurities or air bubbles.

For most of this text, the object of interest is assumed to be two dimensional and the electrodes are treated as point-like boundary current sources. The former is in practice an

accurate simplification only in some symmetric measurement settings, while the latter is a second-order approximation of the complete electrode model (CEM) [11, 28] as the size of the electrodes goes to zero [18]. Although both of these assumptions are essential for our mathematical analysis, neither of them seems to ruin the practical applicability of the results, as demonstrated by our numerical examples (cf section 5).

To be more precise, one of the two electrodes is held fixed, while the other moves around the examined object in a sweeping motion. Unit current is maintained between the electrodes, and the corresponding relative potential difference is measured as a function of the position of the dynamic electrode. This measurement ideally provides a single function defined on the object boundary, dubbed *sweep data* in [14]. According to the material in [14], the sweep data are the (real-valued) trace of a holomorphic function living in the exterior of the conductivity inhomogeneities.

In this work, we derive a holomorphic asymptotic expansion for the (extended) sweep data with respect to the size of an inhomogeneity that is composed of a finite number of Lipschitz inclusions with constant conductivity levels. This can be seen as a generalization to a less regular framework of an analogous result for *backscatter data* in [16]; see [3, 9] for more comprehensive studies of such asymptotics. (Backscatter data are obtained by moving a single small probe of two electrodes along the object boundary, resulting arguably in lower current densities in the interior of the examined object than the sweep measurement, cf [14, 18].) The leading-order term in the asymptotic expansion of the sweep data turns out to be a rational function that has poles (only) inside the inclusions.

The above observation makes it possible to adopt from [16] an idea for locating several small inclusions: certain Laurent–Padé approximants are computed for the sweep data and the corresponding poles are considered as estimates for the positions of the inhomogeneities. We also introduce a novel method for estimating the *net conductivity effects* of the inclusions by manipulating algebraically the residues of the Laurent–Padé approximants; the net conductivity effect is a measure for the 'strength' of an inclusion obtained by combining its size and conductivity contrast in a natural way (cf (3.23)). Although the algorithm is built for the unit disk—as is the one in [16]—our implementation generalizes straightforwardly to any bounded smooth and simply connected planar domain with the help of conformal mappings. For completeness, it should be mentioned that related algorithms have previously been applied to the *standard measurement* of EIT, e.g., in [4, 6, 7, 13, 15, 23].

The functionality of the reconstruction method is demonstrated by numerical experiments based on simulated data. In addition to testing the algorithm with two-dimensional domains and point electrodes, we also consider three-dimensional cylindrical objects and electrodes of realistic size in the framework of the CEM, which has been shown to model real-life measurements up to measurement precision [11, 28]. Furthermore, we test the method with inclusions of varying conductivities, which is a setting not covered by the background theory.

This text is organized as follows. In section 2, we introduce the theoretical framework and sweep data. Section 3 generalizes a factorization of the relative Neumann-to-Dirichlet map from [16] to our less regular framework and subsequently introduces the asymptotic expansion of the sweep data. The reconstruction algorithm is presented in section 4 and tested numerically in section 5.

2. The setting and sweep data

Let $D \subset \mathbb{R}^n$, $n \geqslant 2$, be a simply connected and bounded domain with a $\mathscr{C}^\infty$-boundary; our main theoretical results will be formulated only for the two-dimensional case, but some

interesting intermediate theorems are valid independently of n. Throughout this work, it is assumed that the conductivity $\sigma \in L^\infty(D)$, $\sigma \geqslant c > 0$ almost everywhere, takes the form

$$\sigma(x) = \begin{cases} \kappa_j(x) & \text{if } x \in \Omega_j, \quad j = 1, \ldots, m, \\ 1 & \text{otherwise,} \end{cases}$$

where $\Omega_1, \ldots, \Omega_m$ are the bounded Lipschitz domains with connected complements, such that

$$\overline{\Omega}_i \cap \overline{\Omega}_j = \emptyset \quad \text{for all } i \neq j \qquad \text{and} \qquad \Omega := \bigcup_{j=1}^{m} \Omega_j \subset\subset D. \tag{2.1}$$

The term *inclusion* can refer to either Ω_j or the pair (Ω_j, κ_j).

Let us consider the boundary value problem

$$\nabla \cdot (\sigma \nabla u) = 0 \quad \text{in } D, \qquad \frac{\partial u}{\partial \nu} = f \quad \text{on } \partial D, \tag{2.2}$$

where ν is the exterior unit normal of ∂D. According to the material in, e.g., [19, appendix], for any boundary current density f in

$$H^s_\diamond(\partial D) = \{g \in H^s(\partial D) \mid \langle g, 1\rangle_{\partial D} = 0\}, \qquad s \in \mathbb{R}, \tag{2.3}$$

problem (2.2) has a unique solution u in $(H^{\min\{1, s+3/2\}}(D) \cap H^1_{\mathrm{loc}}(D))/\mathbb{C}$. Here and in what follows, $\langle \cdot, \cdot \rangle_{\partial D} : H^s(\partial D) \times H^{-s}(\partial D) \to \mathbb{C}$ denotes the dual evaluation between Sobolev spaces on ∂D.

The Neumann-to-Dirichlet map

$$\Lambda_\sigma : f \mapsto u|_{\partial D}, \qquad H^s_\diamond(\partial D) \to H^{s+1}(\partial D)/\mathbb{C} \tag{2.4}$$

is well defined and bounded for every $s \in \mathbb{R}$ (cf, e.g., [19, appendix]). The same also applies to the reference Neumann-to-Dirichlet map

$$\Lambda_{\mathbb{1}} : f \mapsto u_{\mathbb{1}}|_{\partial D}, \qquad H^s_\diamond(\partial D) \to H^{s+1}(\partial D)/\mathbb{C},$$

where $u_{\mathbb{1}} \in H^{s+3/2}(D)/\mathbb{C}$ is the unique solution of (see [25, chapter 2, remark 7.2])

$$\Delta u_{\mathbb{1}} = 0 \quad \text{in } D, \qquad \frac{\partial u_{\mathbb{1}}}{\partial \nu} = f \quad \text{on } \partial D. \tag{2.5}$$

Because σ is identically 1 in some (interior) neighborhood of ∂D, it follows that $u - u_{\mathbb{1}}$ is smooth near the boundary ∂D, and the relative Neumann-to-Dirichlet map

$$\Lambda_\sigma - \Lambda_{\mathbb{1}} : H^{-s}_\diamond(\partial D) \to H^s(\partial D)/\mathbb{C} \tag{2.6}$$

is bounded for any fixed $s \in \mathbb{R}$ (cf, e.g., [19, appendix]).

Let us then consider the two-dimensional case, i.e. $n = 2$, and a specific localized current pattern, namely $\delta_z - \delta_{z_0} \in H^{-1/2-\epsilon}_\diamond(\partial D)$, $\epsilon > 0$, with $z, z_0 \in \partial D$ and δ_y denoting the delta distribution located at y on ∂D. Due to the boundedness of the boundary operator (2.6) and since $\delta_z - \delta_{z_0}$ has zero mean in the sense of (2.3), the quantity

$$\varsigma_\sigma(z) = \langle (\delta_z - \delta_{z_0}), (\Lambda_\sigma - \Lambda_{\mathbb{1}})(\delta_z - \delta_{z_0}) \rangle_{\partial D} \tag{2.7}$$

is well defined. The function $\varsigma_\sigma : \partial D \to \mathbb{R}$ is what we call the sweep data of EIT. According to [18], such data can be approximated in practice as follows: unit current is maintained between two small (but finite) electrodes at z_0 and z while the latter is moved along ∂D in a sweeping motion. The corresponding potential difference between the electrodes is recorded as a function of z, and the actual sweep-type data are finally obtained by subtracting the corresponding measurement in the case when $\sigma \equiv 1$. In the framework of the CEM [11, 28], the discrepancy between such a realistic data set and ς_σ is of the order of $O(d^2)$, where $d > 0$ is the length of the electrodes; see [18, theorem 2.1] for the details.

If D is interpreted as a part of the complex plane, the sweep data are the trace of a holomorphic function. In order to concretize this claim, let us introduce

$$\Omega^* := \{\zeta \in \mathbb{C} : 1/\overline{\zeta} \in \Omega\} = \{\zeta \in \mathbb{C} : \zeta\overline{\xi} - 1 = 0 \text{ for some } \xi \in \Omega\},$$

i.e. the reflection (inversion) of Ω with respect to the unit circle, and set

$$\tilde{\Omega} := \mathbb{C} \setminus (\overline{\Omega} \cup \overline{\Omega^*}).$$

Let us first assume that D is a disk.

Theorem 2.1. *If D is the open unit disk, the sweep data $\varsigma_\sigma : \mathbb{C} \supset \partial D \to \mathbb{R} \subset \mathbb{C}$ of (2.7) extend as a holomorphic function to $\tilde{\Omega}$, with the symmetry*

$$\overline{\varsigma_\sigma(\zeta)} = \varsigma_\sigma(1/\overline{\zeta}) \tag{2.8}$$

for all $\zeta \in \tilde{\Omega}$.

Proof. The assertion is a simplified version of [14, theorem 4.1] combined with the reflection principle. □

The above theorem can be generalized in a slightly weaker form for a general bounded, smooth and simply connected domain D.

Corollary 2.2. *The sweep data $\varsigma_\sigma : \mathbb{C} \supset \partial D \to \mathbb{R} \subset \mathbb{C}$ of (2.7) extend as a holomorphic function to $D \setminus \overline{\Omega}$.*

Proof. The claim follows directly from [14, theorem 4.3], and is based on the extension for the unit disk given by theorem 2.1 and the fact that sweep data can be transported between different domains with the help of conformal maps [14, theorem 3.2]. (To make this last statement a bit more transparent, let Φ be a conformal map of D onto the unit disk B. Then, $\varsigma_\sigma \circ \Phi^{-1}|_{\partial B}$ gives the sweep data corresponding to the unit disk and the conductivity $\sigma \circ \Phi^{-1}$; see [14, section 3].) □

3. Asymptotic expansion of sweep data

In this section, it is assumed that the conductivities of the inclusions $\kappa_1, \ldots, \kappa_m$ are constants. To begin with, we will generalize a factorization of the relative Neumann-to-Dirichlet map from [16] to our framework of Lipschitz inclusions (and more general domains), then we will write an asymptotic expansion for the corresponding (relative) energy form and finally, we will deduce the holomorphic asymptotics of the sweep data. For now, we assume that $D \subset \mathbb{R}^n$, $n \geqslant 2$, is smooth, bounded and simply connected, but in section 3.3, we will restrict our attention to the case $n = 2$.

3.1. Factorization of $\Lambda_\sigma - \Lambda_{\mathbb{1}}$

Let us introduce the quotient space

$$L^2(\partial\Omega)/\mathbb{C}^m := (L^2(\partial\Omega_1)/\mathbb{C}) \oplus \ldots \oplus (L^2(\partial\Omega_m)/\mathbb{C})$$

and note that its dual is realized by

$$L^2_*(\partial\Omega) := L^2_\diamond(\partial\Omega_1) \oplus \ldots \oplus L^2_\diamond(\partial\Omega_m).$$

Recall that $u_{\mathbb{1}}$ denotes the solution of (2.5) and consider the linear operator

$$A_\Omega : f \mapsto \left.\frac{\partial u_{\mathbb{1}}}{\partial \nu}\right|_{\partial\Omega}, \qquad H^s_\diamond(\partial D) \to L^2_*(\partial\Omega), \tag{3.1}$$

which is well defined and bounded due to the interior regularity theory for elliptic partial differential equations [25], the fact that the exterior unit normal field of $\partial\Omega$ is in $L^\infty(\partial\Omega)$, and the Gauss divergence theorem (cf [12]). Furthermore, let

$$\lambda_\Omega : L^2_*(\partial\Omega) \to L^2(\partial\Omega)/\mathbb{C}^m \tag{3.2}$$

be the Neumann-to-Dirichlet map corresponding to the Laplacian and $\Omega = \bigcup_{j=1}^m \Omega_j$ (cf [12]).

We denote by $N(\cdot,\cdot) : D \times D \to \mathbb{R}$ the Neumann–Green function for D (cf [3]), i.e.

$$\Delta N(\cdot, y) = -\delta_y \quad \text{in } D, \qquad \frac{\partial N(\cdot, y)}{\partial \nu} = -\frac{1}{|\partial D|} \quad \text{on } \partial D,$$

together with the normalizing condition $\int_{\partial D} N(x,\cdot)\mathrm{d}s_x = 0$. The double-layer operator $K^N_\Omega : L^2(\partial\Omega) \to L^2(\partial\Omega)$, corresponding to Ω and the Neumann–Green function, is defined via (cf [3, section 2.3])

$$\big(K^N_\Omega \psi\big)(y) = \text{p.v.} \int_{\partial\Omega} \frac{\partial N}{\partial \nu_x}(x,y)\psi(x)\mathrm{d}s_x, \qquad y \in \partial\Omega. \tag{3.3}$$

It is straightforward to see that the adjoint of K^N_Ω is given by

$$(K^{N*}_\Omega \psi)(y) = \text{p.v.} \int_{\partial\Omega} \frac{\partial N}{\partial \nu_y}(x,y)\psi(x)\mathrm{d}s_x, \qquad y \in \partial\Omega.$$

Moreover, it follows, e.g., from the jump formulae for double-layer potentials [3] that K^N_Ω maps the span of the characteristic functions $\chi_{\partial\Omega_1}, \ldots, \chi_{\partial\Omega_m}$ onto itself, and thus it can be considered as a bounded map from $L^2(\partial\Omega)/\mathbb{C}^m$ to itself; due to duality, this means that K^{N*}_Ω is well defined and bounded from $L^2_*(\partial\Omega)$ to itself. With these tools in hand, we have the following factorization (cf [1]).

Theorem 3.1. *If each inclusion Ω_j, $j = 1, \ldots, m$, is a bounded $\mathscr{C}^1$-domain with a connected complement, then the difference Neumann-to-Dirichlet map can be factorized as*

$$\Lambda_\sigma - \Lambda_{\mathbb{1}} = A'_\Omega \big(E - K^N_\Omega\big)^{-1} \lambda_\Omega A_\Omega, \tag{3.4}$$

where A_Ω is as in (3.1), A'_Ω is its dual, λ_Ω is the Neumann-to-Dirichlet map of (3.2) and $E : L^2(\partial\Omega)/\mathbb{C}^m \to L^2(\partial\Omega)/\mathbb{C}^m$ is a 'diagonal' operator defined by

$$Ev|_{\partial\Omega_j} = \frac{1}{2}\frac{1+\kappa_j}{1-\kappa_j} v|_{\partial\Omega_j}.$$

In addition, the operator $\big(E - K^N_\Omega\big)^{-1} : L^2(\partial\Omega)/\mathbb{C}^m \to L^2(\partial\Omega)/\mathbb{C}^m$ is bounded.

Proof. The assertion follows by slightly modifying the material in [16]; see also [3]. The full proof can be found in [27, theorem 6.10]. Note that D is assumed to be the unit disk in [16], but this plays no essential role in the proof. □

Remark 3.2. The *only* reason for not introducing factorization (3.4) directly for Lipschitz inclusions is that the operators K^N_Ω and K^{N*}_Ω are no longer compact [3, section 2.3.3] and the invertibility of $E - K^N_\Omega$ cannot be deduced from the Riesz–Fredholm theory, as in [16]; see also [27, theorem 6.10]. The surjectivity of a closely related operator is proven in [3, section 2.3.3] for (connected) Lipschitz Ω. However, we do not stretch this matter any further here because the validity of factorization (3.4) can be proven for *small enough* Lipschitz inclusions by a straightforward perturbation argument (see corollary 3.3 below).

The operator K_Ω^N can be interpreted as an $m \times m$ 'matrix of operators'

$$K_\Omega^N = \begin{bmatrix} K_{1,1} & \cdots & K_{1,m} \\ \vdots & \ddots & \vdots \\ K_{m,1} & \cdots & K_{m,m} \end{bmatrix}$$

acting on a vector $\psi = [\psi|_{\partial\Omega_1}, \ldots, \psi|_{\partial\Omega_m}]^T$ of L^2-functions on the corresponding inclusion boundaries. With this in mind, let us introduce the standard double-layer operator corresponding to $\Omega_j \subset \mathbb{R}^n$, i.e. $K_{\Omega_j} : L^2(\partial\Omega_j) \to L^2(\partial\Omega_j)$ defined as [3]

$$(K_{\Omega_j}\phi)(y) = \frac{1}{\omega_n}\text{p.v.}\int_{\partial\Omega_j} \frac{(x-y)\cdot \nu_x}{|y-x|^n}\phi(x)\,\mathrm{d}s_x, \qquad y \in \partial\Omega_j,$$

with the adjoint

$$(K_{\Omega_j}^*\phi)(y) = \frac{1}{\omega_n}\text{p.v.}\int_{\partial\Omega_j} \frac{(y-x)\cdot \nu_y}{|y-x|^n}\phi(x)\,\mathrm{d}s_x, \qquad y \in \partial\Omega_j,$$

where ω_n denotes the area of the unit sphere in $\mathbb{R}^n$. As for K_Ω^N and its adjoint above, it can be reasoned that K_{Ω_j} is in fact bounded from $L^2(\partial\Omega_j)/\mathbb{C}$ to itself and $K_{\Omega_j}^*$ from $L^2_\diamond(\partial\Omega_j)$ to itself. Furthermore, after setting $K_\Omega = \text{diag}(K_{\Omega_j}, \ldots, K_{\Omega_m})$, it is not hard to see that

$$K_\Omega^N = -K_\Omega + R_\Omega, \tag{3.5}$$

where each integral operator constituting the matrix R_Ω has an almost everywhere bounded kernel $R_{ij}(\cdot,\cdot) : \partial\Omega_j \times \partial\Omega_i \to \mathbb{R}$ such that $R_{ij}(x,\cdot)$ has a $\mathscr{C}^\infty$-smooth extension to some proper neighborhood of Ω_i for every $1 \leqslant i, j \leqslant m$ and almost every $x \in \partial\Omega_j$. Analogously, the kernels of the adjoint R_Ω^*, say $R_{ij}^*(\cdot,\cdot) : \partial\Omega_j \times \partial\Omega_i \to \mathbb{R}$, are also bounded almost everywhere, and $R_{ij}^*(\cdot, y)$ has a smooth extension to some proper neighborhood of Ω_j for every $1 \leqslant i, j \leqslant m$ and almost every $y \in \partial\Omega_i$. Moreover, the derivatives of the extensions of $R_{ij}(x,\cdot)$ and $R_{ij}(\cdot, y)$ can be bounded independently of $x \in \partial\Omega_j$ and $y \in \partial\Omega_i$, respectively (cf, e.g., [3]). Note that the only source of irregularity in R_{ij} (respectively in R_{ij}^*) is the unit normal field of $\partial\Omega_j$ (resp. of $\partial\Omega_i$).

From now on, assume that the inclusions are given by

$$\Omega_j = \Omega_j(\varepsilon) := x_j + \varepsilon O_j, \qquad j = 1, \ldots, m,$$

where x_j are distinct points in D and the 'shapes' O_j are bounded Lipschitz domains which have connected complements and contain the origin. The corresponding piecewise constant conductivity is denoted by $\sigma = \sigma(\varepsilon)$. Let $\varepsilon > 0$ be sufficiently small so that assumptions (2.1) are satisfied.

Corollary 3.3. *For sufficiently small $\varepsilon > 0$, factorization (3.4) holds for the arbitrary bounded Lipschitz shapes O_j, $j = 1, \ldots, m$. Moreover, as an operator from $L^2(\partial\Omega)/\mathbb{C}^m$ to itself,*

$$\left(E - K_{\Omega(\varepsilon)}^N\right)^{-1} = L^{-1} + \tilde{R}_\varepsilon, \tag{3.6}$$

where the inverse of $L = \text{diag}(L_1, \ldots, L_m) := E + K_{\Omega(\varepsilon)}$ is bounded independently of ε and

$$\|\tilde{R}_\varepsilon\| \leqslant C\varepsilon^n \tag{3.7}$$

for some $C > 0$.

Proof. As already discussed in remark 3.2, the sole concern is the invertibility of the operator $E - K_\Omega^N : L^2(\partial\Omega)/\mathbb{C}^m \to L^2(\partial\Omega)/\mathbb{C}^m$. The adjoint of this operator can be written as

$$E^* - K_\Omega^{N*} = L^* - R_\Omega^* : L^2_*(\partial\Omega) \to L^2_*(\partial\Omega), \tag{3.8}$$

where $L^* = \operatorname{diag}(L_1^*, \dots, L_m^*)$, and it is known that each operator

$$L_j^* = E^*|_{\partial\Omega_j} + K_{\Omega_j}^* = \frac{1}{2}\frac{1+\kappa_j}{1-\kappa_j} I + K_{\Omega_j}^*, \qquad j = 1, \dots, m,$$

is invertible on $L^2_\diamond(\partial\Omega_j)$ [3, section 2.3.3].

A simple change of variables shows that for any $\phi \in L^2_\diamond(\partial\Omega_j)$ and almost every $y \in \partial O_j$,

$$(K^*_{\Omega_j(\varepsilon)}\phi)(\varepsilon y + x_j) = \frac{1}{\omega_n}\,\text{p.v.}\int_{\partial O_j} \frac{(y-x)\cdot \nu_y}{|y-x|^n}\phi(\varepsilon x + x_j)\,\mathrm{d}s_x = (K^*_{O_j}\varphi)(y), \tag{3.9}$$

where $\phi \mapsto \varphi := \phi(\varepsilon\cdot + x_j)$ defines a linear isomorphism of $L^2_\diamond(\partial\Omega_j(\varepsilon))$ onto $L^2_\diamond(\partial O_j)$ for any $\varepsilon > 0$. As a consequence, the operator norm

$$\begin{aligned}
\|(L_j^*)^{-1}\|^2 &= \sup_{\phi\in L^2_\diamond(\partial\Omega_j(\varepsilon))\setminus\{0\}} \frac{\|\phi\|^2_{L^2(\partial\Omega_j(\varepsilon))}}{\|L_j^*\phi\|^2_{L^2(\partial\Omega_j(\varepsilon))}} \\
&= \sup_{\phi\in L^2_\diamond(\partial\Omega_j(\varepsilon))\setminus\{0\}} \frac{\varepsilon^{n-1}\int_{\partial O_j}|\phi(\varepsilon x + x_j)|^2\,\mathrm{d}s_x}{\varepsilon^{n-1}\int_{\partial O_j}|\frac{1}{2}\frac{1+\kappa_j}{1-\kappa_j}\phi(\varepsilon x + x_j) + (K^*_{\Omega_j(\varepsilon)}\phi)(\varepsilon x + x_j)|^2\,\mathrm{d}s_x} \\
&= \sup_{\varphi\in L^2_\diamond(\partial O_j)\setminus\{0\}} \frac{\int_{\partial O_j}|\varphi|^2\,\mathrm{d}s}{\int_{\partial O_j}|\frac{1}{2}\frac{1+\kappa_j}{1-\kappa_j}\varphi + (K^*_{O_j}\varphi)|^2\,\mathrm{d}s} = \left\|\left(\frac{1}{2}\frac{1+\kappa_j}{1-\kappa_j}I + K^*_{O_j}\right)^{-1}\right\|^2
\end{aligned}$$

is independent of ε. By duality, the same is true for each L_j, and consequently $L : L^2(\partial\Omega)/\mathbb{C}^m \to L^2(\partial\Omega)/\mathbb{C}^m$ is invertible with $\|L^{-1}\|$ independent of ε.

On the other hand, the (ε-independent) kernels R^*_{ij} of the integral operators in $R^*_{\Omega(\varepsilon)}$ can be extended smoothly with respect to the first variable. In consequence, by Taylor's theorem, for any $\psi \in L^2_\diamond(\partial\Omega_j(\varepsilon))$ with small enough $\varepsilon > 0$, it holds that

$$\begin{aligned}
\left|\int_{\partial\Omega_j(\varepsilon)} R^*_{ij}(x,y)\psi(x)\,\mathrm{d}s_x\right| &= \left|\int_{\partial\Omega_j(\varepsilon)} (x - x_j)\cdot\nabla_x R^*_{ij}(x_j + \eta(x,y), y)\psi(x)\,\mathrm{d}s_x\right| \\
&\leqslant C\varepsilon\int_{\partial\Omega_j(\varepsilon)}|\psi|\,\mathrm{d}s \leqslant C\varepsilon^{1+\frac{n-1}{2}}\|\psi\|_{L^2(\partial\Omega_j(\varepsilon))}
\end{aligned}$$

for almost every $y \in \partial\Omega_i$ and with $\nabla_x R^*_{ij}$ denoting the gradient of $R^*_{ij}(\cdot,\cdot)$ with respect to its first variable. Here, $|\eta(x,y)| \leqslant |x - x_j| \leqslant \varepsilon\,\operatorname{diam}(O_j)$ for all $x \in \partial\Omega_j$ and almost all $y \in \partial\Omega_i$. It easily follows that

$$\|R_{\Omega(\varepsilon)}\| = \|R^*_{\Omega(\varepsilon)}\| \leqslant C\varepsilon^n,$$

where $R_{\Omega(\varepsilon)}$ is treated as an operator from $L^2(\partial\Omega)/\mathbb{C}^m$ to itself. For sufficiently small $\varepsilon > 0$, it thus holds in particular that $\|L^{-1}R_{\Omega(\varepsilon)}\| \leqslant \frac{1}{2}$, and then (3.6) and (3.7) follow from the Neumann series representation of the inverse. □

3.2. Asymptotics of an energy form

Next, we will introduce an asymptotic expansion of the bilinear energy form induced by $\Lambda_\sigma - \Lambda_{\mathbb{1}}$ with respect to the size of the inclusions $\varepsilon > 0$. To this end, we need to resort to polarization tensors [3].

Definition 3.4. *Let O be a Lipschitz inclusion with constant conductivity $\kappa > 0$, $\kappa \neq 1$. Its Pólya–Szegö polarization tensor is the $n \times n$ matrix*

$$M(\kappa, O) = \int_{\partial O} \nu_x \left(\left(\frac{1}{2}\frac{1+\kappa}{1-\kappa}I - K_O\right)^{-1} y^T\right)(x)\,\mathrm{d}s_x, \tag{3.10}$$

where the (inverse) operator in parentheses is applied to the row vector y^T component-wise and, after left multiplication by the column vector ν_x, the resulting matrix is integrated element-wise.

Note that the above definition is unambiguous even though $(\frac{1}{2}\frac{1+\kappa}{1-\kappa}I - K_O)^{-1}$ is treated as an operator from $[L^2(\partial O)/\mathbb{C}]^n$ to itself: the integral of $\nu_x a^T$ over ∂O is the zero matrix for any constant vector $a \in \mathbb{R}^n$ due to Green's theorem (cf, e.g., [12]).

Example 3.5. Let $B_R \subset \mathbb{R}^2$ be a disk of radius $R > 0$ and $\kappa \neq 1$ positive. Then for all $x, y \in \partial B_R$, $x \neq y$, it holds that [3, section 2.2]

$$\frac{(x-y)\cdot \nu_x}{|x-y|^2} = \frac{1}{2R}.$$

In consequence, K_{B_R} vanishes as an operator from $L^2(\partial B_R)/\mathbb{C}$ to itself and

$$\left(\frac{1}{2}\frac{1+\kappa}{1-\kappa}I - K_{B_R}\right)^{-1} = 2\frac{1-\kappa}{1+\kappa}I : \ L^2(\partial B_R)/\mathbb{C} \to L^2(\partial B_R)/\mathbb{C}.$$

Thus, the corresponding polarization tensor can easily be computed in a closed form:

$$M(\kappa, B_R) = 2\pi R^2 \frac{1-\kappa}{1+\kappa}\begin{bmatrix} 1 & 0 \\ 0 & 1 \end{bmatrix}. \tag{3.11}$$

Combining corollary 3.3 with definition 3.4 leads to an asymptotic expansion for the bilinear (relative) energy form

$$\langle \cdot, (\Lambda_\sigma - \Lambda_{\mathbb{1}})\cdot \rangle : \ H^s_\diamond(\partial D) \times H^s_\diamond(\partial D) \to \mathbb{C}, \qquad s \in \mathbb{R}. \tag{3.12}$$

Although the following theorem corresponds to [16, (4.22)], we reproduce the proof here due to the Lipschitz (ir)regularity of the inclusions and the use of L^2-spaces on their boundaries. The theorem could also be deduced from the more general result [2, theorem 1.1].

Theorem 3.6. *Let $f, g \in H^s_\diamond(\partial D)$. The bilinear form (3.12) satisfies*

$$\langle g, (\Lambda_{\sigma(\varepsilon)} - \Lambda_{\mathbb{1}})f\rangle = \varepsilon^n \sum_{j=1}^m \nabla u_{g,\mathbb{1}}(x_j)^T M(\kappa_j, O_j)\nabla u_{f,\mathbb{1}}(x_j) + O(\varepsilon^{n+1}), \tag{3.13}$$

where $u_{f,\mathbb{1}}$ and $u_{g,\mathbb{1}}$ are the solutions of (2.5) for the currents f and g, respectively.

Proof. From (3.1) and the interior regularity theory for elliptic partial differential equations [25], it follows that

$$(A_\Omega g)(x) = \nu_x \cdot \nabla u_{g,\mathbb{1}}(x_j) + r_{j,\varepsilon}(x)$$

and

$$(\lambda_\Omega A_\Omega f)(x) = u_{f,\mathbb{1}}(x) = u_{f,\mathbb{1}}(x_j) + (x - x_j)\cdot \nabla u_{f,\mathbb{1}}(x_j) + r'_{j,\varepsilon}(x)$$

for almost all $x \in \partial\Omega_j$. Here, $\|r_{j,\varepsilon}\|_{L^\infty(\partial\Omega_j)} \leqslant C\varepsilon\|g\|_{H^s(\partial D)}$ and $\|r'_{j,\varepsilon}\|_{L^\infty(\partial\Omega_j)} \leqslant C\varepsilon^2\|f\|_{H^s(\partial D)}$ with some $C > 0$ independent of $\varepsilon > 0$ and $j = 1, \ldots, m$. We define $B_1 : H^s_\diamond(\partial D) \to L^2_*(\partial\Omega)$ and $B_2 : H^s_\diamond(\partial D) \to L^2(\partial\Omega)/\mathbb{C}^m$ component-wise via

$$(B_1 g|_{\partial\Omega_j})(x) = \nu_x \cdot \nabla u_{g,\mathbb{1}}(x_j),$$
$$(B_2 f|_{\partial\Omega_j})(x) = (x - x_j)\cdot \nabla u_{f,\mathbb{1}}(x_j).$$

Then the operator norm estimates

$$\|A_{\Omega(\varepsilon)} - B_1\| \leqslant C\varepsilon^{1+\frac{n-1}{2}}, \qquad \|\lambda_{\Omega(\varepsilon)}A_{\Omega(\varepsilon)} - B_2\| \leqslant C\varepsilon^{2+\frac{n-1}{2}},$$

and

$$\|A_{\Omega(\varepsilon)}\| \leqslant C\varepsilon^{\frac{n-1}{2}}, \qquad \|B_1\| \leqslant C\varepsilon^{\frac{n-1}{2}}$$

are satisfied. By a change of variables, it is also easy to see that

$$\|\lambda_{\Omega(\varepsilon)}\| = \varepsilon \max_{j=1,\ldots,m} \|\lambda_{O_j}\|.$$

Corollary 3.3 yields that, for sufficiently small $\varepsilon > 0$,

$$\langle g, (\Lambda_\sigma - \Lambda_{\mathbb{1}})f\rangle = \int_{\partial\Omega} (A_\Omega g)((E - K^N_{\Omega(\varepsilon)})^{-1}\lambda_\Omega A_\Omega f)\,\mathrm{d}s = \int_{\partial\Omega} (B_1 g)(L^{-1}B_2 f)\,\mathrm{d}s + \mathcal{E},$$

where

$$\mathcal{E} = \int_{\partial\Omega} ((A_\Omega g)(\tilde{R}_\varepsilon \lambda_\Omega A_\Omega f) + ((A_\Omega - B_1)g)(L^{-1}\lambda_\Omega A_\Omega f) + (B_1 g)(L^{-1}(\lambda_\Omega A_\Omega - B_2)f))\,\mathrm{d}s.$$

By applying the Cauchy–Schwarz inequality to each term in the integral $\mathcal{E}$, minding the relevant operator norms, it follows that

$$|\mathcal{E}| \leqslant C\varepsilon^{n+1}\|f\|_{H^s(\partial D)}\|g\|_{H^s(\partial D)}.$$

Moreover, the leading term satisfies

$$\int_{\partial\Omega} (B_1 g)(L^{-1}B_2 f)\,\mathrm{d}s_x = \sum_{j=1}^m \nabla u_{g,\mathbb{1}}(x_j)^T \int_{\partial\Omega_j(\varepsilon)} \nu_x \big(L_j^{-1}(y - x_j)^T\big)(x)\,\mathrm{d}s_x \nabla u_{f,\mathbb{1}}(x_j),$$

where

$$\begin{aligned}
&\int_{\partial\Omega_j(\varepsilon)} \nu_x (L_j^{-1}(y - x_j)^T)(x)\,\mathrm{d}s_x \\
&\qquad = \int_{\partial\Omega_j(\varepsilon)} \nu_x \left(\left(\frac{1}{2}\frac{1+\kappa_j}{1-\kappa_j} I + K_{\Omega_j(\varepsilon)}\right)^{-1} (y - x_j)^T\right)(x)\,\mathrm{d}s_x \\
&\qquad = \varepsilon^{n-1} \int_{\partial O_j} \nu_{\hat{x}} \left(\left(\frac{1}{2}\frac{1+\kappa_j}{1-\kappa_j} I + K_{\Omega_j(\varepsilon)}\right)^{-1} (y - x_j)^T\right)(\varepsilon\hat{x} + x_j)\,\mathrm{d}s_{\hat{x}} \\
&\qquad = \varepsilon^{n-1} \int_{\partial O_j} \nu_{\hat{x}} \left(\left(\frac{1}{2}\frac{1+\kappa_j}{1-\kappa_j} I + K_{O_j}\right)^{-1} (\varepsilon y)^T\right)(\hat{x})\,\mathrm{d}s_{\hat{x}} \\
&\qquad = \varepsilon^n M(\kappa_j, O_j).
\end{aligned}$$

The penultimate step follows from a change of variables similar to (3.9). □

3.3. Holomorphic expansion of sweep data

In the rest of this section, it is assumed that $n = 2$. To be able to compare the asymptotic expansion of theorem 3.6 with the known complex analytic properties of the sweep data (cf theorem 2.1 and corollary 2.2), we need to write (3.13) in complex variables for the special case $f = g = \delta_z - \delta_{z_0}$ with $z, z_0 \in \partial D$.

To begin with, assume that $D = B$ is the open unit disk and note that the gradient of the corresponding background solution $u^z_{\mathbb{1}}$ of (2.5) with $f = \delta_z - \delta_{z_0}$ is (cf, e.g., [14])

$$\nabla u^z_{\mathbb{1}}(x) = \frac{1}{\pi}\left(\frac{x - z_0}{|x - z_0|^2} - \frac{x - z}{|x - z|^2}\right), \qquad x \in D. \tag{3.14}$$

We identify the mapping $(x, z) \mapsto \nabla u_{\mathbb{I}}^{z}(x)$ (from $D \times \partial D \subset \mathbb{R}^2 \times \mathbb{R}^2$ to $\mathbb{R}^2$) with a complex function $(\xi, \zeta) \mapsto v(\xi, \zeta)$, which is a map from $D \times \partial D \subset \mathbb{C} \times \mathbb{C}$ to $\mathbb{C}$. To be more precise,

$$v(\xi, \zeta) = \frac{1}{\pi}\left(\frac{\xi - \zeta_0}{(\xi - \zeta_0)\overline{(\xi - \zeta_0)}} - \frac{\xi - \zeta}{(\xi - \zeta)\overline{(\xi - \zeta)}}\right) = \frac{1}{\pi}\left(\frac{1}{\overline{\xi} - \overline{\zeta}_0} - \frac{\zeta}{\zeta\overline{\xi} - 1}\right), \tag{3.15}$$

where we took advantage of the fact that $|\zeta|^2 = 1$ and $\zeta_0 \in \partial D$ is the complex number corresponding to z_0 (we denote such a relationship as $\zeta_0 \hat{=} z_0$ in the following). For fixed $\xi \in D$, $v(\xi, \cdot)$ extends as a holomorphic function to the complement of the set $\{\xi\}^* := \{1/\overline{\xi}\}$; let us denote this extension by $w_1(\xi, \cdot) : \mathbb{C} \setminus \{\xi\}^* \to \mathbb{C}$. Analogously, the complex conjugate of v, i.e.

$$\overline{v(\xi, \zeta)} = \frac{1}{\pi}\left(\frac{1}{\xi - \zeta_0} - \frac{1}{\xi - \zeta}\right),$$

can be extended as a holomorphic function, say $w_2(\xi, \cdot)$, to $\mathbb{C} \setminus \{\xi\}$. It thus follows that also the real and imaginary parts of $v(\xi, \cdot)$ have holomorphic extensions

$$v_1(\xi, \cdot) = \frac{1}{2}(w_1(\xi, \cdot) + w_2(\xi, \cdot)), \qquad v_2(\xi, \cdot) = \frac{1}{2\mathrm{i}}(w_1(\xi, \cdot) - w_2(\xi, \cdot)) \tag{3.16}$$

to $\mathbb{C} \setminus (\{\xi\} \cup \{\xi\}^*)$. We denote $V = V_{\zeta_0} = [v_1, v_2]^T$, where the subindex is sometimes used to remind about the dependence on the static electrode location $\zeta_0 \in \partial D$.

Let us then adopt the short notation $M_j = M(\kappa_j, O_j)$ and introduce the meromorphic function

$$\begin{aligned} \varsigma_\varepsilon(\zeta) &:= \varepsilon^2 \sum_{j=1}^{m} V(\xi_j, \zeta)^T M_j V(\xi_j, \zeta) \\ &= \frac{\varepsilon^2}{4\pi^2} \sum_{j=1}^{m} \left(\overline{\beta}_j \left(\frac{1}{\overline{\xi}_j - \overline{\zeta}_0} - \frac{\zeta}{\zeta\overline{\xi}_j - 1} \right)^2 + \beta_j \left(\frac{1}{\xi_j - \zeta_0} - \frac{1}{\xi_j - \zeta} \right)^2 \right. \\ &\quad \left. + 2\alpha_j \left(\frac{1}{\overline{\xi}_j - \overline{\zeta}_0} - \frac{\zeta}{\zeta\overline{\xi}_j - 1} \right) \left(\frac{1}{\xi_j - \zeta_0} - \frac{1}{\xi_j - \zeta} \right) \right) \end{aligned} \tag{3.17}$$

that is defined on $\mathbb{C} \setminus \bigcup_{j=1}^{m}(\{\xi_j\} \cup \{\xi_j\}^*)$ with $\xi_j \hat{=} x_j$. Here, $\alpha = M_{11} + M_{22}$ and $\beta = M_{11} - M_{22} + 2\mathrm{i}M_{12}$ for a generic polarization tensor M. Now, recall the holomorphically extended sweep data from theorem 2.1 and let us state the main theoretical results of this work.

Theorem 3.7. *Let D be the open unit disk. Then, the sweep data allow the asymptotic expansion*

$$\varsigma_{\sigma(\varepsilon)} = \varsigma_\varepsilon + O(\varepsilon^3) \qquad \text{as } \varepsilon \to 0^+ \tag{3.18}$$

uniformly on any compact subset of $\mathbb{C} \setminus \bigcup_{j=1}^{m}(\{\xi_j\} \cup \{\xi_j\}^*)$.

Proof. For the actual measurement $\varsigma_{\sigma(\varepsilon)}|_{\partial D}$, the assertion follows directly from the definition of sweep data (2.7) and theorem 3.6.

To see that (3.18) holds in fact uniformly on any compact subset of $\mathbb{C} \setminus \bigcup_{j=1}^{m}(\{\xi_j\} \cup \{\xi_j\}^*)$, one needs to restate the proof of [16, theorem 5.2] for sweep data. We recall the inclusion-wise-defined logarithmic function

$$g_{\zeta_0}(\xi, \zeta) = \frac{1}{2\pi}\left(\log\frac{|\zeta_0 - \xi|^2}{1 - \overline{\xi}\zeta} + \log\frac{\zeta - \xi_j}{\zeta - \xi}\right) \qquad \text{for } \xi \in \partial\Omega_j, \quad j = 1, \ldots, m,$$

from [14, (4.2)], with the unessential modification that the static electrode is now at ζ_0 instead of $1 \in \mathbb{C}$. It is straightforward to check that

$$V_{\zeta_0}(\xi, \zeta) = \nabla_x g_{\zeta_0}(\xi, \zeta)$$

for any $\xi \in \partial\Omega$. Here, $\xi = \xi(x) = x_1 + \mathrm{i}x_2 \in \mathbb{C}$ is treated as a function of the corresponding $x = (x_1, x_2) \in \mathbb{R}^2$. Due to the analytic properties of g_{ζ_0} and corollary 3.3 (cf [14, section 4], [19, lemma 4.1], [27, theorem 6.20]), the holomorphic extension of $\varsigma_{\sigma(\varepsilon)}$ to $\mathbb{C}\setminus\overline{(\Omega(\varepsilon)\cup\Omega(\varepsilon)^*)}$ can be written as

$$\varsigma_{\sigma(\varepsilon)}(\zeta) = \int_{\partial\Omega} \frac{\partial}{\partial\nu_x} g_{\zeta_0}(\xi(x),\zeta)\left((E-K_\Omega^N)^{-1}\lambda_\Omega \frac{\partial}{\partial\nu} g_{\zeta_0}(\xi(\cdot),\zeta)\right)(x)\,\mathrm{d}s_x. \tag{3.19}$$

Now the arguments in the proof of theorem 3.6 can be repeated, replacing both $u_{f,\mathbb{1}}$ and $u_{g,\mathbb{1}}$ with g_{ζ_0}, to show that (3.18) is valid on an arbitrary compact subset of $\mathbb{C}\setminus\bigcup_{j=1}^m(\{\xi_j\}\cup\{\xi_j\}^*)$. □

In order to handle a general smooth, bounded and simply connected domain $D \subset \mathbb{C}$, let Φ be a conformal map that sends D onto the open unit disk B; note that the restriction $\Phi|_{\partial D}$ also defines a smooth diffeomorphism of ∂D onto ∂B [26, section 3.3]. We define a new, Φ-dependent meromorphic function

$$\varsigma_\varepsilon^\Phi(\zeta) = \varepsilon^2 \sum_{j=1}^m V_{\Phi(\zeta_0)}(\Phi(\xi_j),\zeta)^T (J_\Phi(\xi_j) M_j J_\Phi(\xi_j)^T) V_{\Phi(\zeta_0)}(\Phi(\xi_j),\zeta) \tag{3.20}$$

for $\zeta \in \mathbb{C}\setminus\bigcup_{j=1}^m(\{\Phi(\xi_j)\}\cup\{\Phi(\xi_j)\}^*)$ and with $\zeta_0 \in \partial D$ denoting the static electrode position. By slight abuse of the notation, $J_\Phi(\xi_j)$ denotes here the Jacobian matrix of Φ—treated as a map from $D \subset \mathbb{R}^2$ to $B \subset \mathbb{R}^2$—evaluated at $x_j \hat{=} \xi_j$.

Corollary 3.8. *Let $D \subset \mathbb{C}$ be a smooth, bounded and simply connected domain. Then, the sweep data have the asymptotic expansion*

$$\varsigma_{\sigma(\varepsilon)} = \varsigma_\varepsilon^\Phi \circ \Phi + O(\varepsilon^3) \qquad \text{as } \varepsilon \to 0^+ \tag{3.21}$$

uniformly on any compact subset of $\overline{D}\setminus\bigcup_{j=1}^m\{\xi_j\}$.

Proof. It follows from the line of reasoning in the proof of [14, theorem 3.2] that the background solution $u_{\mathbb{1}}^z := u_{f,\mathbb{1}}$, with $f = \delta_z - \delta_{z_0}$, needed in the definition of $A_\Omega(\delta_z - \delta_{z_0}) \in L^2_*(\partial\Omega)$ can be given as $u_{\mathbb{1}}^z = u_{\mathbb{1}}^{\Phi(z)} \circ \Phi$, where $u_{\mathbb{1}}^{\Phi(z)}$ is the solution of (2.5) with $f = \delta_{\Phi(z)} - \delta_{\Phi(z_0)}$ and D replaced by the unit disk B. In consequence, the holomorphic extension of the sweep data, $\varsigma_{\sigma(\varepsilon)} : \overline{D}\setminus\overline{\Omega(\varepsilon)} \to \mathbb{C}$, is given by (3.19) if $g_{\zeta_0}(\xi,\zeta)$ is replaced by $g_{\Phi(\zeta_0)}(\Phi(\xi),\Phi(\zeta))$. Again, the arguments in the proof of theorem 3.6 can be repeated to prove convergence, and the chain rule shows that the leading-order term is indeed equal to $\varsigma_\varepsilon^\Phi \circ \Phi$. □

Corollary 3.9. *Let $\Omega'(\varepsilon) = \xi + \varepsilon O \subset \mathbb{C}$, $\xi \in D$ be a disk-shaped inclusion of constant conductivity $\kappa > 0$. Then the leading-order term $\varsigma_\varepsilon^\Phi$ of the asymptotic expansion (3.21) for the sweep data (with the inhomogeneity consisting of (Ω',κ) and possibly other inclusions) has a first-order pole at $\Phi(\xi)$ with the residue*

$$\mathrm{Res}(\varsigma_\varepsilon^\Phi, \Phi(\xi)) = \det J_\Phi(\xi)\,|\Omega'|\frac{2}{\pi^2}\frac{1-\kappa}{1+\kappa}\left(\frac{1}{\overline{\Phi(\xi)}-\overline{\Phi(\zeta_0)}} - \frac{\Phi(\xi)}{|\Phi(\xi)|^2-1}\right), \tag{3.22}$$

where $|\Omega'|$ denotes the area of Ω'.

Proof. The claim follows by combining (3.17) and (3.20) with example 3.5, and bearing in mind that $J_\Phi J_\Phi^T = (\det J_\Phi) I$ due to the Cauchy–Riemann equations. □

Corollary 3.9 demonstrates that the knowledge of the conformal map Φ and the leading-order term $\varsigma_\varepsilon^\Phi$ (everywhere in B) allows stable reconstruction of certain information about the size and conductivity level of a disk-shaped inclusion. This is an important observation for the reconstruction algorithm of section 4, and it merits the definition of a new quantity.

Definition 3.10. *Let $\Omega' \subset \mathbb{C}$ be a bounded Lipschitz inclusion with homogeneous conductivity $\kappa > 0$. Its net conductivity effect is defined as*

$$\rho(\Omega', \kappa) = |\Omega'| \frac{\kappa - 1}{\kappa + 1}. \tag{3.23}$$

In particular, there exists a lower limit

$$r_{\min}(\rho_0) := \inf\{r : |\rho(B_r, \kappa)| = \rho_0;\ \kappa, r > 0\} = \sqrt{\frac{\rho_0}{\pi}} \tag{3.24}$$

for the radius $r > 0$ of a discoidal inclusion B_r with absolute net conductivity effect $\rho_0 > 0$. This limit radius corresponds to an inclusion with vanishing or infinite conductivity, i.e. a perfect insulator or conductor.

4. Algorithmic implementation

In this section, we introduce an algorithm for reconstructing the locations of multiple (small) inclusions in the conductivity σ of an otherwise homogeneous unit disk $D = B \subset \mathbb{R}^2$ from (noisy) sweep data; see remark 4.3 at the end of this section for a generalization to the case of more general domains. The method is inspired by the holomorphic extension property of sweep data (see theorem 2.1) and the complex asymptotic expansion (3.18). The algorithm is a modified and amended version of the reconstruction method devised by Hanke in [16] for backscatter data. In particular, the estimation of net conductivity effects is not tackled in [16]; in fact, it is not clear how this should be done in the case of backscatter data.

The algorithm constructs a Laurent–Padé approximant, a complex rational function, which reproduces the sweep data on ∂D. It is anticipated that the poles of the approximant locate the inclusions and, moreover, that the corresponding residues can be used to compute estimates for the net conductivity effects (3.23). There is no theoretical result that would appropriately justify this, but the numerical experiments presented in section 5 indicate that the method works as desired.

4.1. Laurent–Padé approximants

Let us first define the Laurent–Padé approximants that constitute an integral part of our reconstruction algorithm.

Definition 4.1. *A Laurent–Padé approximant of type $[L/M]$ for a formal Laurent series $\sum_{j=-\infty}^{\infty} c_j z^j$ is the (complex) function*

$$\frac{p^{[L/M]}(z)}{q^{[L/M]}(z)} = \frac{\sum_{j=-L}^{L} p_j z^j}{\sum_{j=-M}^{M} q_j z^j} = \frac{\alpha^+(z)}{\beta^+(z)} + \frac{\alpha^-(z^{-1})}{\beta^-(z^{-1})}, \tag{4.1}$$

where $\alpha^{\pm}(z) = \sum_{j=0}^{\max(L,M)} \alpha_j^{\pm} z^j$, $\beta^{\pm}(z) = \sum_{j=0}^{M} \beta_j^{\pm} z^j$ are the polynomials whose coefficients satisfy, respectively, (4.4) and (4.3) below. (The order symbol $[L/M]$ is omitted from the coefficients p_j, q_j for clarity.) [5, section 7.4]

Let us introduce the Hankel matrices

$$H_{[L/M],\pm} = \begin{bmatrix} c'_{\pm(L-M+1)} & \cdots & c'_{\pm L} \\ \vdots & \ddots & \vdots \\ c'_{\pm L} & \cdots & c'_{\pm(L+M-1)} \end{bmatrix}, \tag{4.2}$$

where $c_0' = \frac{1}{2}c_0$ and $c_j' = c_j$ for all $j \neq 0$. Then,

$$\begin{bmatrix} \beta_M^{\pm} \\ \vdots \\ \beta_1^{\pm} \end{bmatrix} = -H_{[L/M],\pm}^{-1} \begin{bmatrix} c_{\pm(L+1)} \\ \vdots \\ c_{\pm(L+M)} \end{bmatrix} \tag{4.3}$$

and

$$\alpha_k^{\pm} = \sum_{j=0}^{\min(k,M)} \beta_j^{\pm} c_{k-j}', \qquad k = 0, \ldots, \max(L, M), \tag{4.4}$$

define the coefficients of the polynomials in the Laurent–Padé approximants of type $[L/M]$. If either of the matrices $H_{[L/M],\pm}$ is singular, it is said that the corresponding Laurent–Padé approximant does not exist. This possibility is not considered here in any detail; if a matrix should appear severely ill-conditioned in our numerical computations, the reconstruction algorithm is considered to have failed.

The most important quality of Laurent–Padé approximants is that they match the corresponding formal Laurent series up to order $L+M$. For more information on this property and other aspects of Laurent–Padé approximants, we refer to [5].

4.2. Sweep data reconstruction method

The following corollary summarizes the key complex analytic properties of sweep data for the case $D = B$.

Corollary 4.2. *The sweep data $\varsigma_\sigma : \partial D \to \mathbb{R}$ have a unique holomorphic extension to $\tilde{\Omega}$, that is, up to the boundary of the inclusions (and their reflections). This extension satisfies the inversion symmetry (2.8) and is uniquely determined by its Laurent coefficients on ∂D, or equivalently by the Fourier coefficients of $\varsigma_\sigma|_{\partial D} : [0, 2\pi) \to \mathbb{R}$. Moreover, $\varsigma_{\sigma(\varepsilon)}$ allows the asymptotic expansion (3.18) with respect to the size $\varepsilon > 0$ of homogeneous Lipschitz inclusions; the corresponding leading-order term ς_ε is a meromorphic function that has poles only inside the inclusions (and their reflections).*

On the other hand, the idea of Laurent–Padé approximants is to 'mimic' a given Laurent series, and each such approximant defines a meromorphic function in $\mathbb{C}$. It is also easy to see that, if calculated from the Laurent/Fourier coefficients of noncomplex data, the Laurent–Padé approximants exhibit symmetry (2.8). From the inverse problem point of view, it is important that low-order approximants are computed from low-order Fourier coefficients, which are relatively insensitive to noise—a well-known regularizing property exploited by a plethora of numerical methods. This information suggests using low-order Laurent–Padé approximants for regularized reconstruction of the holomorphic extension of sweep data from noisy measurements.

The following reconstruction method is based on a set of hypothesized properties of the Laurent–Padé approximants of sweep data, stemming from the characteristics of the complex small inclusion expansion (3.18). In particular, it is anticipated that the poles of the approximants reside near the inclusions (and their reflections outside the unit disk), as is the case for the leading-order term in (3.18). For each (first-order) pole $\xi \in D$ of an approximant $f = p^{[L/M]}/q^{[L/M]}$, the corresponding *effect*

$$\mu(f, \xi) = \frac{-\pi^2}{2} \frac{\operatorname{Res}(f, \xi)}{\frac{1}{\bar{\xi} - \bar{\zeta}_0} - \frac{\xi}{|\xi|^2 - 1}} \tag{4.5}$$

is viewed as an estimate for the net conductivity effect of (a part of) an inclusion close to ξ (cf (3.23) and (3.22) with $\Phi = \mathrm{Id}$). More precisely, if the poles $\xi_1, \ldots, \xi_k$ are located 'near' an inclusion Ω' (of any shape), it is expected that

$$\rho(\Omega', \kappa) \approx \mu_{\mathrm{cl}}(f, \{\xi_1, \ldots, \xi_k\}) := \sum_{j=1}^{k} \mu(f, \xi_j). \tag{4.6}$$

It must be stressed that the suggested relationship between the inclusions and the poles in the approximants has not been proven to exist. Moreover, even for the exact leading-order term (3.17) of the asymptotic expansion, estimate (4.6) is theoretically justified only for discoidal inclusions; cf corollary 3.9 with $\Phi = \mathrm{Id}$. Further considerations for closing these theoretical gaps are omitted in this work. Instead, the usefulness of the method is assessed on the grounds of numerical experiments, which indeed support these hypotheses.

Formal extension of (4.1) yields that, when $L < M$ (respectively $L > M$), the $[L/M]$ Laurent–Padé approximant has a root (resp. a pole) of multiplicity $|L - M|$ at $z = 0$. Consequently, approximants of type $[(M-2)/M]$ were used in [16] because the leading-order term of the asymptotic expansion for backscatter data has a double root at the origin. However, (3.17) has no persistent pole nor root at the origin, meaning that the most natural choice for sweep data is the $[M/M]$ approximants.

In our numerical experiments, it is assumed that the sweep data are given as (noisy) samples $\varsigma_1, \ldots, \varsigma_N$ at N equispaced points

$$x_j = \exp\left(\frac{2\pi \mathrm{i}(j-1)}{N}\right), \qquad j = 1, \ldots, N,$$

on the unit circle. Approximations of the Fourier coefficients of the 'underlying' sweep data ς_σ, which coincide with the corresponding Laurent coefficients (cf [16]), are computed by taking the discrete Fourier transform of $\varsigma_1, \ldots, \varsigma_N$. Note that the maximum sensible degree of an $[M/M]$ Laurent–Padé approximant for these kinds of data is $M = \lfloor N/4 \rfloor$.

For noisy data, our choice of M is based on the *Morozov discrepancy principle*

$$\left| \left(\frac{p^{[M/M]}(x_j)}{q^{[M/M]}(x_j)} - \varsigma_j \right)_{j=1}^{N} \right| \approx \mathbb{E} \left| \left(\varsigma(x_j) - \varsigma_j\right)_{j=1}^{N} \right| \tag{4.7}$$

at the measurement points, that is, a proper choice of M is such that the residual is approximately equal to the expected value of the error in a suitable noise model (cf [24]). This is somewhat different from the approach in [16], where the error is studied in terms of the Fourier coefficients. In the case of ideal data, i.e. with no model error or measurement noise, we choose the value of M that produces the 'best' reconstruction in order to study the limits for the proposed reconstruction method.

The final task is locating the poles and calculating the corresponding residues for the rational function (4.1) on the basis of the coefficients p_j, q_j. This can be done by first transforming (4.1) to a proper fraction by formal polynomial (long) division. Then one should find the roots of the denominator polynomial $\tilde{q}(z)$ and finally calculate the residues as in, e.g., [22, vol I, section 9]. In terms of linear algebra, finding the roots corresponds to determining the eigenvalues for the companion matrix of the polynomial.

Numerically, finding poles and residues is generally an ill-posed problem, especially in the case of multiple poles (poles of order greater than 1). In fact, even constructing the Laurent–Padé approximants from the Laurent coefficients is a relatively unstable numerical problem [5]. These stability issues are not studied deeply here. It is merely anticipated that the regularization originating from the discrete Fourier transform suffices for obtaining reasonable low-order approximations. For example, the presence of multiple poles in the numerical computations can be considered unlikely (cf [16]).

Remark 4.3. The above algorithm generalizes easily to the case of a smooth, bounded and simply connected planar domain D, assuming that a conformal mapping of D onto the open unit disk B is available. Indeed, the composite map $\varsigma_{\sigma(\varepsilon)} \circ \Phi^{-1}$ has $\varsigma_\varepsilon^\Phi$ as the leading-order term of its asymptotic expansion according to corollary 3.8. Thus, one can first apply the above algorithm to the transformed data $\varsigma_{\sigma(\varepsilon)} \circ \Phi^{-1}|_{\partial B}$ to find the poles and corresponding residues of a suitable Laurent–Padé approximant in B. Subsequently, the poles can be mapped back inside D by Φ^{-1} to deduce the positions of the inclusions. Moreover, the corresponding clustered effects (4.6) give estimates for the net conductivity effects of the original inclusions in D after scaling by $\det J_\Phi$ evaluated at the respective inclusion locations (cf (3.22)). The testing of this generalized algorithm is left for future studies.

5. Numerical experiments

In this section, we test numerically the reconstruction method introduced in section 4. We will first consider ideal sweep data produced by point electrodes and with no artificial noise added. Subsequently, we will move the focus of our attention on simulated noisy CEM measurements corresponding to realistic parameter values.

5.1. Experiments with ideal data

Figure 1(a) shows a conductivity phantom σ comprising two inclusions: a resistive disk and a conductive ellipse. The corresponding ideal sweep data $\varsigma_\sigma : [0, 2\pi) \to \mathbb{R}$ are depicted in figure 1(b). They were computed (at $N = 320$ equispaced points on ∂D) using a boundary element method as in [14, 20] and can be considered highly accurate. The plot also features the Laurent–Padé approximant of type [3/3] that deviates from the sweep data by less than 10^{-5} and is visually indistinguishable. Moreover, figure 1(d) illustrates the discrepancy between the (holomorphically continued) sweep data and the chosen approximant in the exterior of the inclusions; the extended sweep data were computed by using (a variant of) the formula [14, (4.3)], which can be evaluated with the help of layer potentials in the case of homogeneous inclusions. It is apparent that the Laurent–Padé approximant provides an accurate estimate of the sweep data away from the inhomogeneity (and its reflections with respect to ∂D), but this correspondence degenerates as one approaches the inclusion boundaries. In this and all other examples of this subsection, the object of interest D is the unit disk and the static electrode is at the polar angle $\theta_0 = 0$, i.e. at the boundary point $z_0 = (1, 0)$.

Figure 1(c) illustrates the poles and effects (4.5) of the approximant. Each pole-effect pair (ξ, μ) is depicted as a circle that is centered at ξ and whose radius corresponds to the lower limit $r_{\min}(|\mu|)$ in (3.24), and a direction pointer for the argument $\angle\mu$. As estimates of net conductivity effects (3.23), left pointing markers indicate resistive and right pointing markers indicate conductive inclusions. Effects (4.5) of the poles are, from top to bottom, $\mu_1 = -0.0038 + 0.0000\mathrm{i}$, $\mu_2 = 0.0044 - 0.0005\mathrm{i}$ and $\mu_3 = 0.0054 + 0.0004\mathrm{i}$. The first one closely matches the net conductivity effect $\rho_{\text{disk}} = -0.003\,77$ of the discoidal inclusion, and the 'clustered effect' $\mu_{\text{cl}} = \mu_2 + \mu_3 = 0.0097 - 0.0001\mathrm{i}$ is also a decent approximation of $\rho_{\text{ellipse}} = 0.0101$. To be more precise, the relative error between the actual net conductivity effect and the estimated one $|\rho - \mu_{\text{cl}}|/|\rho|$ is less than 4% for both inclusions (cf (4.6)).

Figure 2 shows a similar experiment with a more complicated conductivity phantom. The number of measurement points on ∂D remains the same, but this time a high-order Laurent–Padé approximant of type [16/16] is utilized. The pole-effect pairs of the approximant are illustrated in figure 2(c). In this case, there are effects with considerable imaginary components and effects of opposite phases inside a single inclusion. It is thus clear that the effects of

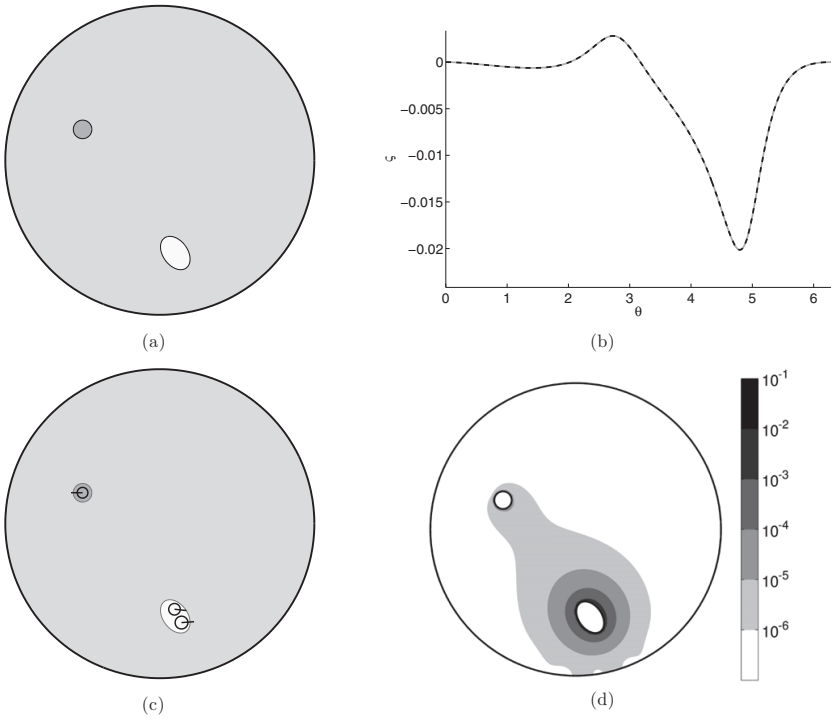

Figure 1. Reconstruction of a simple conductivity phantom from ideal sweep data. (a) Conductivity phantom. The disk has conductivity $\kappa = 1/2$ and the ellipse $\kappa = 2$. (b) Sweep data (solid gray) and the corresponding Laurent–Padé approximant with $M = 3$ (dashed). (c) Reconstruction with $M = 3$. (d) Discrepancy between the Laurent–Padé approximant and the analytically continued sweep data.

individual poles do not necessarily correspond to the resistivity/conductivity of an inclusion, but the relationship between the inclusions and poles is more complicated. However, when the effects of the poles near an inclusion are accumulated, the resulting clustered effect μ_{cl} is still a decent approximation of the corresponding net conductivity effect. Figure 2(d) shows a clusterization of the poles and depicts the resulting pairs $(\xi_{\mathrm{cl}}, \mu_{\mathrm{cl}})$, where ξ_{cl} are computed as weighted averages of the poles in the cluster. In this case, $|\mu_{\mathrm{cl}} - \rho|/|\rho| < 8\%$ for all inclusions.

It should also be noted that the locations of the poles in figure 2(c) provide some information about the shapes of the inclusions. Particularly, the poles seem to locate the vertices of the polygonal inclusions, and the main axis of the ellipse. Keeping in mind corollary 3.9 and the theory of analytic continuation, it is not surprising that the disk seems to be represented by a single pole at its center; see the numerical results in [14] for analogous conclusions.

As yet, our conductivity phantoms have consisted of homogeneous Lipschitz inclusions, as required by the theoretical results in section 3. The next example aims to show that the homogeneity assumption is not essential for the reconstruction algorithm. Sweep data for the conductivity phantom in figure 3(a) were computed by solving the relative potential

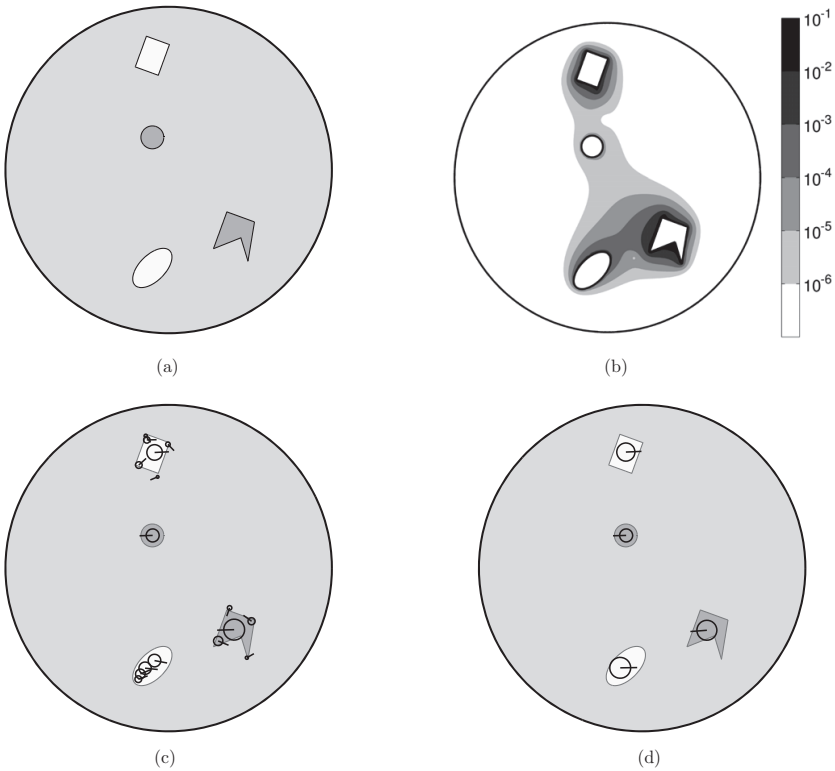

Figure 2. Reconstruction of a complicated conductivity phantom from ideal sweep data. (a) Conductivity phantom. The box and the ellipse have $\kappa = 2$. The disk and the concave polygon are resistive with $\kappa = 1/2$. (b) Discrepancy between the [16/16] Laurent–Padé approximant and the analytically continued sweep data. (c) Reconstruction with $M = 16$. (d) Clusterized reconstruction.

$w = u_{\sigma,f} - u_{\mathbb{1},f} \in H^1(D)/\mathbb{C}$, i.e. the difference of the solutions to (2.2) and (2.5), from the variational equation

$$\int_D \sigma \nabla w \cdot \nabla v \, \mathrm{d}x = \int_D (1-\sigma) \nabla u_{\mathbb{1},f} \cdot \nabla v \, \mathrm{d}x \qquad \text{for all } v \in H^1(D)/\mathbb{C} \tag{5.1}$$

for the relevant current patterns $f = \delta_z - \delta_{z_0}$ using the finite element method (FEM); see (2.7) and [17, (5.5)], and note that $u_{\mathbb{1},f}$ can be given explicitly in the unit disk. The reconstruction of degree $M = 3$, computed from a reduced number $N = 32$ of equispaced measurement points, is shown in figure 3(b). The algorithm locates the inhomogeneities accurately, and the computed effects also provide some information about the distribution of the 'conductivity mass' inside the inclusions.

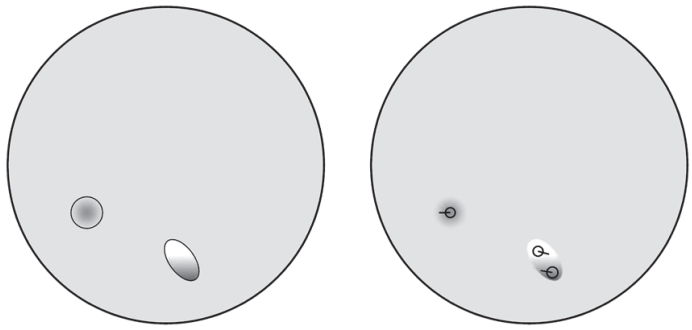

(a) (b)

Figure 3. Reconstruction of inhomogeneous inclusions from $N = 32$ noiseless sweep data samples. (a) Conductivity phantom with a radially symmetric resistive inclusion and an inclusion that changes from conductive (top) to resistive along the vertical axis. (b) Reconstruction with $M = 3$.

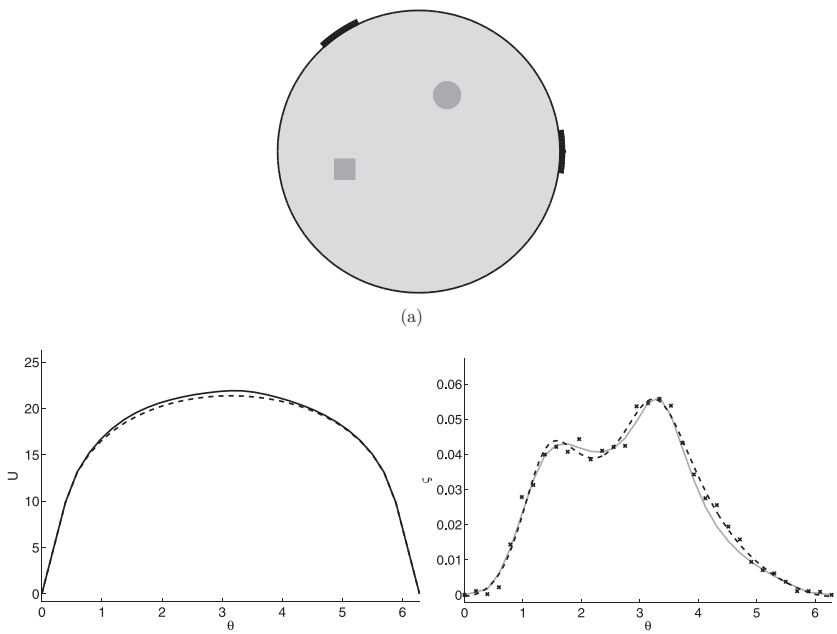

(a) (b) (c)

Figure 4. Conductivity phantom and example CEM sweep data. (a) Conductivity phantom. Both inclusions are perfect insulators (i.e. holes). The thick protruded lines depict the electrodes in an example configuration: the right-hand electrode is static and the left-hand electrode rotating. (b) Measurement with inclusions (solid) and reference measurement (dashed). Their difference is the CEM sweep data. (c) CEM sweep data (solid gray), $N = 32$ noisy samples (x) and the Laurent–Padé approximant of degree $M = 2$ (dashed). The corresponding reconstruction is shown in figure 5(a).

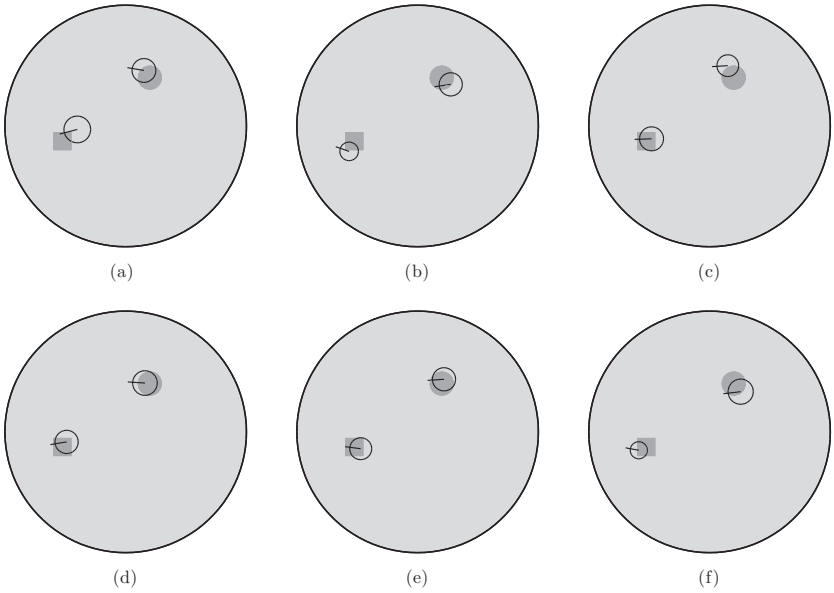

Figure 5. Six reconstructions from different $N = 32$ noisy samples of realistic CEM sweep data, $M = 2$.

5.2. Experiments with CEM data

The following examples test our algorithm in the realistic framework of the CEM. The sweep measurement, as described in section 2, is simulated using two finite-size electrodes and artificial noise is added. To put it very short, unit net current is maintained between the two electrodes while one of them rotates around the object and the corresponding voltage difference is measured as a function of the location of the dynamic electrode. The actual approximate sweep data are then obtained by subtracting the analogous measurement corresponding to a homogeneous object. The noise level is set relative to the magnitude of the (absolute) measurements instead of the magnitude of the (difference) sweep data themselves, which provides a realistic noise model. For more information about the CEM, we refer to [11, 28]; details about FEM simulation of sweep data with finite-size CEM electrodes can be found in [14, section 7].

Figure 4(a) shows the studied measurement configuration in our first CEM experiment. The object D is the unit disk, the background conductivity is 1 and the two inclusions are insulating cavities, i.e. they correspond to the degenerate case $\kappa = 0$ that is modeled by homogeneous Neumann conditions on the respective inclusion boundaries. Each electrode spans an arc of circa 17°, and the contact impedances at the electrode–object interfaces take the value 0.005. These parameters could correspond to, e.g., measurements with a cylindrical water tank of radius 15 cm with rectangular electrodes (cf [21]), assuming that both the electrodes and the cavities are of the same height as the tank itself.

The reference measurement with a homogeneous object and the one with inclusions are shown in figure 4(b); we have chosen $N = 32$, i.e. assume that the voltage difference is

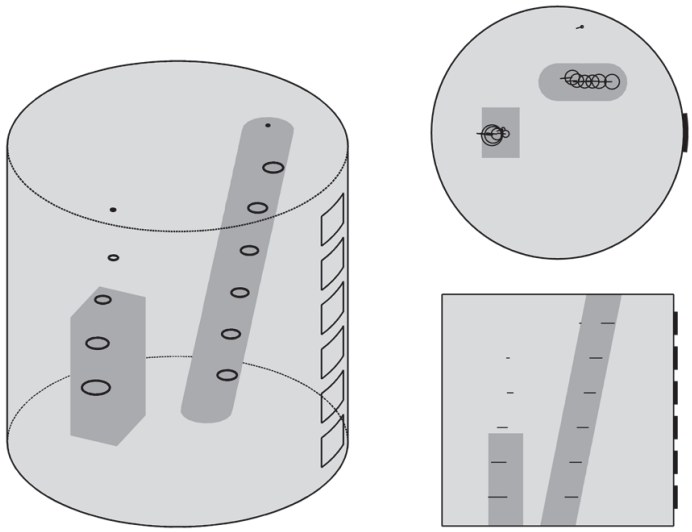

Figure 6. Reconstruction from three-dimensional CEM-simulated sweep measurements on six different height levels. $M = 2$ on each level and the positions of the static electrodes are shown. The radius of the tank is 1 and its height is 2. There are two insulating inclusions inside the tank: a tilted cylinder and a box.

measured at 32 positions of the rotating electrode[1]. A sample of noise with relative level (normal distribution standard deviation) of 0.1% is added to both sets of data, which are subsequently subtracted from each other to simulate the noisy sweep measurement. The amount of noise appears low in figure 4(b), but in the difference data, the relative noise level is dramatically amplified as seen in figure 4(c). Figure 5 shows corresponding reconstructions with six different noise samples. In all cases, the order of the Laurent–Padé approximant is $M = 2$, which approximately satisfies (4.7), without taking into account the (smallish) model error between the CEM and the point electrode model used in the definition of (ideal) sweep data (cf [18]). For all noise realizations, the algorithm finds the approximate inclusion locations and provides relatively accurate estimates of their sizes. (Note that for insulating cavities, the areas of the marker disks give directly estimates for the inclusion sizes since for $\kappa = 0$, the absolute value of the conductivity effect (3.23) is precisely the area of the inclusion in question.)

Our final numerical experiment considers a three-dimensional cylindrical tank of radius 1 and height 2 depicted in figure 6. The contact impedance at the electrode–object interfaces is 0.005 and there are two insulating cavities inside the object. The following measurement is simulated on six different height levels: one electrode is held stationary and another one is 'swept' around the tank along the same height. The difference sweep data (see [14]) are computed by the FEM at 29 points and interpolated at other 2 to obtain a sweep data curve corresponding to 32 equispaced points on the sweep circle at the investigated height. The exact

[1] The value is defined as zero when the electrode positions coincide and computed by interpolation in other cases of overlap (see [14]), which occurs at two positions of the dynamic electrode in this case. As a result, the voltages are actually simulated at 29 positions.

shape of the electrodes is the intersection of the tank surface with a cylinder of height 0.2 and radius 0.15; the central axis of the small cylinder coincides with the tank boundary.

Before computing the reconstruction, the data are multiplied by the height of the electrodes. This scaling corresponds to the (inaccurate) approximation that current only flows parallel to the bottom of the tank, which would reduce the problem to a two-dimensional setting similar to the above two-dimensional CEM example. Finally, the scaled data at each height level are used to compute six individual reconstructions, each of order $M = 2$.

The reconstruction recovers information about the locations of both inclusions on each level. In addition, the cuboid inclusion on the bottom of the tank leaves 'shadow' artifacts on the upper levels. The estimated sizes of the inclusions are systematically too small, apparently due to the model error in the naive reduction to two-dimensional reconstruction problems. This example indicates that the method is not very sensitive to these kinds of systematic errors and might also be feasible for certain inherently three-dimensional settings.

6. Concluding remarks

We have introduced a method for locating multiple inclusions and estimating their conductivity effects from the sweep data of EIT. The algorithm is motivated by an asymptotic expansion of the sweep data, and it forms the reconstruction by considering the poles and corresponding residues of suitable Laurent–Padé approximants (cf [16]). The functionality of the reconstruction technique was demonstrated both with point electrodes in two dimensions and in the realistic framework of the three-dimensional CEM.

Acknowledgments

This work was supported by the Academy of Finland (project 135979) and the Finnish Funding Agency for Technology and Innovation TEKES (contract 40370/08). We would like to thank Professor Jari Kaipio's research group at the University of Eastern Finland (Kuopio) for letting us use their three-dimensional FEM solver for the CEM. We also express our gratitude to Lauri Harhanen for providing us with his boundary element forward solver used for simulating ideal sweep data.

References

[1] Ammari H, Griesmaier R and Hanke M 2007 Identification of small inhomogeneities: asymptotic factorization *Math. Comput.* **76** 1425–48

[2] Ammari H and Kang H 2003 High-order terms in the asymptotic expansions of the steady-state voltage potentials in the presence of conductivity inhomogeneities of small diameter *SIAM J. Math. Anal.* **34** 1152–66

[3] Ammari H and Kang H 2007 *Polarization and Moment Tensors: With Applications to Inverse Problems and Effective Medium Theory* (Berlin: Springer)

[4] Ammari H, Moskow S and Vogelius M S 2003 Boundary integral formulae for the reconstruction of electric and electromagnetic inhomogeneities of small volume *ESAIM Control Optim. Calc. Var.* **9** 49–66

[5] Baker G A and Graves-Morris P 1996 *Padé Approximants* (Cambridge: Cambridge University Press)

[6] Baratchart L, Ben Abda A, Ben Hassen F and Leblond J 2005 Recovery of pointwise sources or small inclusions in 2D domains and rational approximation *Inverse Problems* **21** 51–74

[7] Baratchart L, Leblond J, Mandréa F and Saff E B 1999 How can the meromorphic approximation help to solve some 2D inverse problems for the Laplacian? *Inverse Problems* **15** 79–90

[8] Borcea L 2002 Electrical impedance tomography *Inverse Problems* **18** R99–136

[9] Capdeboscq Y and Vogelius M S 2003 A general representation formula for boundary voltage perturbations caused by internal conductivity inhomogeneities of low volume fraction *Math. Model. Numer. Anal.* **37** 159–73

[10] Cheney M, Isaacson D and Newell J C 1999 Electrical impedance tomography *SIAM Rev.* **41** 85–101
[11] Cheng K-S, Isaacson D, Newell J C and Gisser D G 1989 Electrode models for electric current computed tomography *IEEE Trans. Biomed. Eng.* **36** 918–24
[12] Grisvard P 1985 *Elliptic Problems in Nonsmooth Domains* (Boston, MA: Pitman)
[13] Hakula H and Hyvönen N 2008 Two noniterative algorithms for locating inclusions using one electrode measurement of electric impedance tomography *Inverse Problems* **24** 055018
[14] Hakula H, Hyvönen N and Harhanen L 2011 Sweep data of electrical impedance tomography *Inverse Problems* **27** 115006
[15] Hanke M 2008 On real-time algorithms for the location search of discontinuous conductivities with one measurement *Inverse Problems* **24** 045005
[16] Hanke M 2011 Locating several small inclusions in impedance tomography from backscatter data *SIAM J. Numer. Anal.* **49** 1991–2016
[17] Hanke M, Harhanen L, Hyvönen N and Schweickert E 2012 Convex source support in three dimensions *BIT* **52** 45–63
[18] Hanke M, Harrach B and Hyvönen N 2011 Justification of point electrode models in electrical impedance tomography *Math. Models Methods Appl. Sci.* **21** 1395–413
[19] Hanke M, Hyvönen N and Reusswig S 2011 Convex backscattering support in electric impedance tomography *Numer. Math.* **117** 373–96
[20] Harhanen L and Hyvönen N 2010 Convex source support in half-plane *Inverse Problems Imaging* **4** 429–48
[21] Heikkinen L M, Vilhunen T, West R M and Vauhkonen M 2002 Simultaneous reconstruction of electrode contact impedances and internal electrical properties: II. Laboratory experiments *Meas. Sci. Technol.* **13** 1855–61
[22] Hille E 1982 *Analytic Function Theory* vol 1 (New York: Chelsea)
[23] Kang H and Lee H 2004 Identification of simple poles via boundary measurements and an application of EIT *Inverse Problems* **20** 1853–63
[24] Kirsch A 1996 *An Introduction to the Mathematical Theory of Inverse Problems* (Berlin: Springer)
[25] Lions J-L and Magenes E 1972 *Non-Homogeneous Boundary Value Problems and Applications* vol 1 (Berlin: Springer) (translated from French by P Kenneth)
[26] Pommerenke C 1992 *Boundary Behaviour of Conformal Maps* (Berlin: Springer)
[27] Seiskari O 2011 Locating multiple inclusions from sweep data of electrical impedance tomography *Master's Thesis* Aalto University (http://urn.fi/URN:NBN:fi:aalto-201207022737)
[28] Somersalo E, Cheney M and Isaacson D 1992 Existence and uniqueness for electrode models for electric current computed tomography *SIAM J. Appl. Math.* **52** 1023–40
[29] Uhlmann G 2009 Electrical impedance tomography and Calderón's problem *Inverse Problems* **25** 123011